2018

Analysis of InGaN Quantum Wells with AlGaInN Barriers

Hanlin Fu
Lehigh University

Analysis of InGaN Quantum Wells with AlGaInN Barriers

By

Hanlin Fu

A Thesis

Presented to the Graduate and Research Committee

Of Lehigh University

In Candidacy for the Degree of

Master of Science

in

Electrical Engineering

Lehigh University

December, 2017

This thesis is accepted and approved in partial fulfillment of the requirements for a Master's of Science.

Date: December 14th 2017

Prof. Nelson Tansu, MS Thesis Advisor

Daniel E. '39 and Patricia M. Smith Endowed Chair Professor

Director, Center for Photonics and Nanoelectronics

Prof. Chengshan Xiao

Chair of Electrical and Computer Engineering Department

Acknowledgement

I would first like to thank my advisor Professor Nelson Tansu. I have been working and studying in Prof. Tansu's lab for one year. During this year, I have learned greatly from Prof. Tansu not only in terms of scientific and technical knowledge, but also via profound life principles that he has illustrated by personal example. I benefit a lot from listening to his discussion in the lab. For instance, I now further appreciate the importance of persistence and focus in both study and life, which I aspire to follow in rest of my life. I also do believe that I learn a great deal on the values of honesty, integrity, and responsibility from the experience working together with my advisor. For this, I truly value this learning experience. I appreciate the significant help from Prof.Tansu in my research and I am proud to be his student.

I am also thankful for my family for financially and emotionally supporting me through all my graduate studies in Lehigh University. Whenever I was in trouble and confused about the future, my mother would give me the best comfort and support me in conquering any difficulties. My family always provided me a solid backing and I appreciate all the effort they made to help me.

Finally, I would like to thank all my friends, without whom I could not have gone this far. My lab colleagues Prof. Jonathan Wierer, Dr. Renbo Song, Xiongliang Wei, Wei Sun, Austin Slosberg, Justin Goodrich, Damir Baravoc, Ioannis Fragkos, Onos Ogidi-Ekoko, Syed Ahmed Al Muyeed, Matthew Peart, Qingyang Li, Jiaheng Wu, and Tianfei Song all provide me great help on my research and study. My roommates Lei Li and Yuan Li offer me great enjoyment in life. It's my best fortune to live and study with you.

Table of Contents

List of Figures

List of Tables

Abstract

Various strain-compensated InGaN-AlGaInN quantum well (QW) structures are investigated by self-consistent 6-band ***k·p*** method, which considers valence band mixing, the strain effect, spontaneous and piezoelectric polarizations and the carrier screening effect, for their spontaneous emission and gain properties. The InGaN QW with In-content of 28% is sandwiched by AlGaInN barriers, which are $Al_{0.2}Ga_{0.8}N$, $Al_{0.56}Ga_{0.32}In_{0.12}N$, $Al_{0.72}Ga_{0.13}In_{0.15}N$, $Al_{0.78}Ga_{0.1}In_{0.12}N$, and $Al_{0.82}Ga_{0.1}In_{0.08}N$, with corresponding band gaps of 3.821eV, 4.156eV, 4.465eV, 4.765eV, and 5.065eV, respectively. Both the spontaneous emission spectra and optical gain properties of strain-compensated InGaN–AlGaInN QWs reveal enhancement in comparison to those of conventional InGaN–GN QWs. The enhancement factors of spontaneous emission spectra and peak gain properties for different barrier structures are found to follow a parabolic trend. This indicates differing amounts of improvement of the radiative efficiency for light emitting diodes. This study shows that there is an optimized composition for an AlGaInN barrier layer surrounding an $In_{0.28}Ga_{0.72}N$ quantum well between the bandgaps of 4.156eV and 4.465eV that will obtain the highest spontaneous emission rate and gain properties.

Chapter 1: Introduction

In this chapter, we present a brief introduction of the history and challenges for conventional InGaN-based devices. We introduce the concept of the strain-compensated quantum well and as well as present the organization of this thesis.

1.1 Brief History of Conventional InGaN-Based LEDs

III-Nitride based semiconductors, which are composed of GaN, InN and AlN and their alloys, have changed the world for their amazing ability to emit a wide range of wavelengths in the visible spectrum. The world's first electroluminescence from a GaN film was reported and published in May 1971, by J. I. Pankove et al [1]. H. M. Manasevit reported the first attempt of the growth of thin film nitride samples by MOCVD (metal organic chemical vapor deposition) process which he had pioneered in the same year [2]. In 1984, T. Kawabata et al. reported the first blue GaN LED grown by the MOCVD [3]. The following fundamental breakthrough was the world's first nitride blue LED containing a p-n junction that was presented at a conference in Los Angeles in 1989 [4]. In 1993, S. Nakamura et al. described their advanced p-GaN/n-InGaN/n-GaN double heterojunction (DH) violet LEDs. Their InGaN/GaN DH LED emits blue light at a wavelength of 420nm [5]. In November 1995, Akasaki and Amano reported the fabrication of a novel InGaN/GaN quantum well structure. Their structure is shown in figure 1-1 [6]. Their first observation of stimulated emission from a quantum well structure is shown in figure 1-2 [6]. For the invention of efficient blue light-emitting diodes, which have enabled bright and energy-saving white light sources, Akasaki, Amano, and Nakamura were awarded the 2014 Nobel Prize in

Physics [7]. Nowadays, InGaN based LEDs and lasers have become an irreplaceable technology part for our everyday lives.

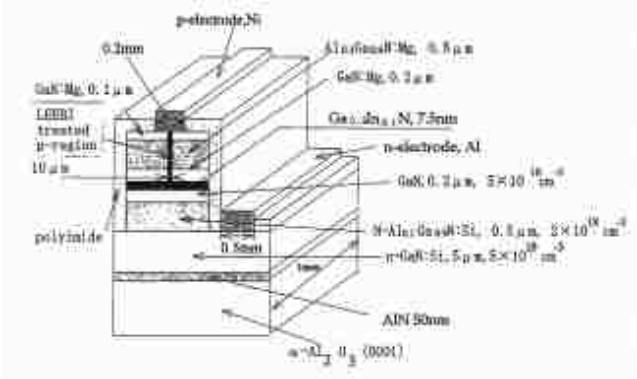

Figure 1-1: Schematic of Akasaki and Amano's MQW nitride structure [6].

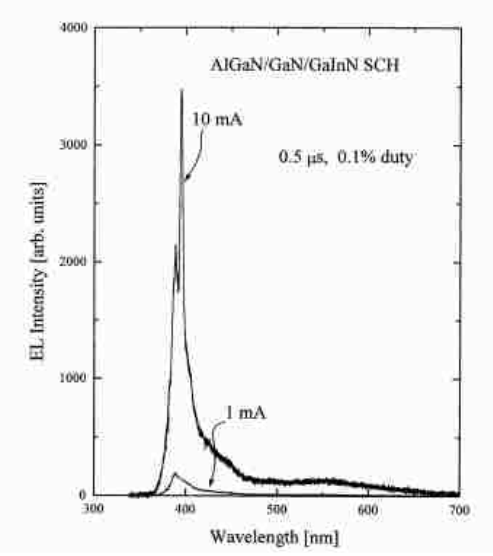

Figure 1-2: The stimulated emission spectra of Akasaki and Amano's first quantum well device [6].

1.2 Challenges of Conventional InGaN Lasers and LEDs

Conventional III-nitride lasers and LEDs are developed based upon the InGaN QW as the active region. There are two major challenges in InGaN QWs. The first is the low electron and hole wave function overlap. This phenomenon is mainly caused by the large spontaneous and piezoelectric polarization in the QW. The second limitation is the high dislocation density caused by the strain-induced lattice mismatch between InGaN and GaN [8]. Previously published reports indicate a significant improvement of optical gain and reduction of the threshold current density by using a strain-compensated InGaN-$Al_{0.2}Ga_{0.8}N$ QW structure with thin ($\sim$1-nm) tensile-strained $Al_{0.2}Ga_{0.8}N$ barriers to surround the compressively strained InGaN QW [8]. Reduction of strain from this barrier structure results in a closer lattice match which in turn causes a lower dislocation density in the lattice. The strain-compensated QW theory involved will be discussed in Section 1.3.

1.3 Strain-Compensated InGaN-AlGaInN Quantum Well

A strain-compensated InGaN-AlGaInN QW is achieved by inserting an AlGaInN barrier which lattice constant smaller than that of GaN to compensate the compressive strain of the InGaN QW. In figure 1-3, we present the transformation process for each layer from an unstrained status to the strain-compensated InGaN-AlGaInN QW. The employment of an AlGaInN barrier results in a reduction of strain energy inside the compressive QW. The concept of strain-compensated QWs was previously applied in InGaAsN QW and InGaAS QW active regions, resulting in high performance 1200-1400nm emitting diode lasers on GaAs substrates [9] - [11].

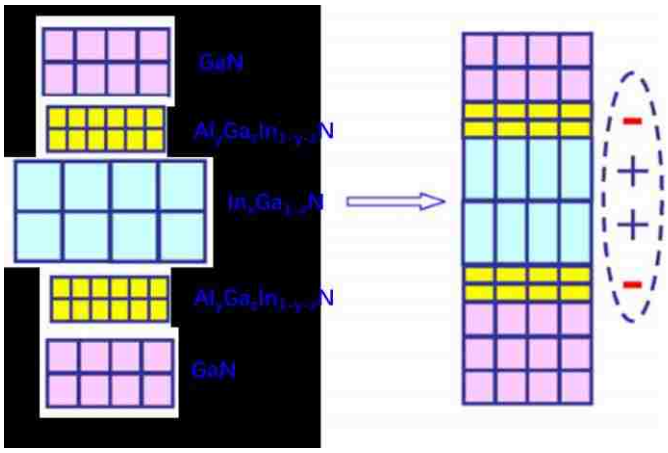

Figure 1-3: Schematic of a strain-compensated InGaN-AlGaInN QW structure with a compressively strained InGaN QW and tensile AlGaInN barriers. [8]

For this work, we will analyze 24-Å $In_{0.28}Ga_{0.72}N$ QWs ($\Delta a/a$~+3.13%) with thin 1-nm barriers of $Al_{0.2}Ga_{0.8}N$ ($\Delta a/a$~-0.47%), $Al_{0.56}Ga_{0.32}In_{0.12}N$ ($\Delta a/a$~-0.013%), $Al_{0.72}Ga_{0.13}In_{0.15}N$ ($\Delta a/a$~ -0.064%), $Al_{0.78}Ga_{0.1}In_{0.12}N$ ($\Delta a/a$~-0.54%), and $Al_{0.82}Ga_{0.1}In_{0.08}N$ ($\Delta a/a$~ -1.09%), with bandgaps of 3.821eV, 4.156eV, 4.465eV, 4.765eV, and 5.065eV, respectively. The employment of larger bandgap barriers of AlGaInN leads to better confinement in the InGaN QW [12]. This strong confinement is important for achieving high performance LEDs and lasers at high temperature [13] - [15].

1.4 Thesis Organization

In this thesis, we will focus on the comparison of various strain-compensated QWs by using different $In_{0.28}Ga_{0.72}N$-$Al_xGa_yIn_{1-x-y}N$ active regions. We will present an elaborate analysis of the band structures, spontaneous emission rates, and gain properties for InGaN QWs with

various AlGaInN barriers. The spontaneous emission and optical gain properties will be calculated under the self-consistent 6-band ***k·p*** formalism [16], [17]. In Chapter 1, we will begin with an introduction to InGaN-based semiconductors, their current technological challenges, and the concept of strain-compensated quantum wells. We will follow this by presenting the 6-band ***k·p*** method under the self-consistent formalism in Chapter 2. The Chapter 3 will present a comparison between the band properties of conventional and various strain-compensated quantum well structures. Finally, in Chapter 4, we will investigate the optical properties of these conventional and strain-compensated quantum wells. In this thesis, we will limit our comparison to two classes of active regions, namely: i) the conventional 24-Å $In_{0.28}Ga_{0.72}N$-GaN QW and ii) the strain-compensated 24-Å $In_{0.28}Ga_{0.72}N$-$Al_{0.2}Ga_{0.8}N$ QW, 24-Å $In_{0.28}Ga_{0.72}N$-$Al_{0.56}Ga_{0.32}In_{0.12}N$ QW, and 24-Å $In_{0.28}Ga_{0.72}N$-$Al_{0.78}Ga_{0.1}In_{0.12}N$. These results will be presented in Chapters 3 and 4.

Chapter 2: Self-Consistent 6-Band *k·p* Method for III-Nitride Semiconductors

In solid-state physics, ***k·p*** perturbation theory is an approximation for the calculation of band structures and optical properties of crystalline solids [18] near the Γ-point. It is developed from Bloch theorem. The Bloch equation can be written as the following:

$$\psi_{n,\mathbf{k}}(\mathbf{x}) = e^{i\mathbf{k}\cdot\mathbf{x}} u_{n,\mathbf{k}}(\mathbf{x}) \qquad (2\text{-}1)$$

where **k** is wave vector, *n* is the discrete index, and $u_{n,\mathbf{k}}$ is a function with the same periodicity as the crystal lattice. This theory is in the framework of the Luttinger-Kohn model. We will present the concept of 6-band ***k·p*** method for wurtzite semiconductors, which was developed by S.L.Chuang et al. [16], [17]. We will also present the formulation of the self-consistent 6-band ***k·p*** method for III-nitride semiconductor following the framework developed in reference 8.

2.1 The Hamiltonian Matrix Elements for 6-Band *k·p* Method

In this thesis, we will utilize the 6-band ***k·p*** method to calculate the band structures of InGaN-AlGaInN strain-compensated QWs. Our calculation will consider valence band mixing, strain effect, spontaneous and piezoelectric polarizations, and the carrier screening effect. We will neglect the coupling between the conduction and valence bands because of the large bandgap. We will assume the conduction band to be parabolic. The valence band structure will be calculated via a 6×6 Hamiltonian matrix [17] in the following form:

$$\mathrm{H}^{v}_{6\times6}(k)=\begin{pmatrix} H^{U}_{3\times3}(k) & 0 \\ 0 & H^{L}_{3\times3}(k) \end{pmatrix} \qquad (2\text{-}2)$$

where $H^{U}_{3\times3}(k)$ and $H^{L}_{3\times3}(k)$ are 3×3 matrices defined as:

$$H^{U}_{3\times3}(k)=\begin{pmatrix} F & K_t & -iH_t \\ K_t & G & \Delta-iH_t \\ iH_t & \Delta+iH_t & \lambda \end{pmatrix} \qquad (2\text{-}3)$$

$$H^{L}_{3\times3}(k)=\begin{pmatrix} F & K_t & iH_t \\ K_t & G & \Delta+iH_t \\ -iH_t & \Delta-iH_t & \lambda \end{pmatrix} \qquad (2\text{-}4)$$

The matrix elements for a strained wurtzite semiconductor are shown as follows:

$$F=\Delta_1+\Delta_2+\lambda+\theta,\quad G=\Delta_1-\Delta_2+\lambda+\theta \qquad (2\text{-}5)$$

$$\lambda=\frac{\hbar^2}{2m_0}(A_1k_z^2+A_2k_t^2)+D_1\varepsilon_{zz}+D_2(\varepsilon_{xx}+\varepsilon_{yy}) \qquad (2\text{-}6)$$

$$\theta=\frac{\hbar^2}{2m_0}(A_3k_z^2+A_4k_t^2)+D_3\varepsilon_{zz}+D_4(\varepsilon_{xx}+\varepsilon_{yy}) \qquad (2\text{-}7)$$

$$K_t=\frac{\hbar^2}{2m_0}A_5k_t^2,\quad H_t=\frac{\hbar^2}{2m_0}A_6k_tk_z,\quad \Delta=\sqrt{2}\Delta_3 \qquad (2\text{-}8)$$

where the strain parameters of the QW and barrier layers are as follows:

$$\varepsilon_{xx}=\varepsilon_{yy}=\frac{a_0-a}{a} \qquad (2\text{-}9)$$

$$\varepsilon_{zz}=-\frac{2C_{12}}{C_{33}}\varepsilon_{xx} \qquad (2\text{-}10)$$

$$\varepsilon_{xy} = \varepsilon_{yz} = \varepsilon_{zx} = 0 \qquad (2\text{-}11)$$

with a_0 and a as the lattice constants of the barrier and well layer, respectively. C_{13} and C_{33} are the stiffness constants of the well layer.

The magnitude of the wave vector k_t can be expressed as $k_t = \sqrt{k_x^2 + k_y^2}$. Note that Δ_1 is the crystal-field split energy and Δ_2 and Δ_3 are for the spin-orbit interaction. The A_i's are the effective mass parameters and the D_i's are the deformation potentials. These parameters are listed in table 3-1 for binary alloys (GaN, InN, and AlN).

2.2 The Spontaneous and Piezoelectric Polarizations Characteristics

The numerical model also considers the spontaneous (P_{SP}) and piezoelectric polarization fields. The spontaneous polarization uses linear interpolation [19] and the piezoelectric polarization can be expressed as follows [20]:

$$P_{PZ} = 2d_{31}(C_{11} + C_{12} - \frac{2C_{13}^2}{C_{33}})\varepsilon_{xx} \qquad (2\text{-}12)$$

where d_{31} and the C's are the piezoelectric coefficient and elastic stiffness coefficients, respectively.

The existence of polarization fields in wurtzite III–Nitride semiconductors results in energy band bending. The electrostatic fields in each layer can be expressed as [21]

$$E_j = \frac{\sum_k l_k P_k / \varepsilon_k - P_j \sum_k l_k / \varepsilon_k}{\varepsilon_j \sum_k l_k / \varepsilon_k} \qquad (2\text{-}13)$$

where P is the total macroscopic polarization, ε is the static dielectric constant, and l is the thickness of each layers.

For the average electric field in the layers, note that the electric field expression in (2-13) needs to satisfy the periodic boundary conditions as follows:

$$\sum_k l_k E_k = 0 \qquad (2\text{-}14)$$

where the summation consists of all layers, including the QW, active regions, and barrier regions.

Note that the total electric field of each layer is the slope for the band lineups.

2.3 Momentum Matrix Elements and Fermi's Golden Rule

The optical transition matrix element relating n^{th}-state in conduction band and m^{th}-state in valence band can be calculated via the envelope functions, as shown below:

• TE-polarization ($\hat{x}$ or $\hat{y}$ polarization)

$$|(M_x)_{nm}^{\sigma}(k_t)|^2 = \frac{|<S|p_x|Z>|^2}{4} \cdot \{<\phi_n|g_m^{(1)}>^2 + <\phi_n|g_m^{(2)}>^2\} \quad \text{for } \sigma=\text{U} \qquad (2\text{-}15a)$$

$$|(M_x)_{nm}^{\sigma}(k_t)|^2 = \frac{|<S|p_x|Z>|^2}{4} \cdot \{<\phi_n|g_m^{(4)}>^2 + <\phi_n|g_m^{(5)}>^2\} \quad \text{for } \sigma=\text{L} \qquad (2\text{-}15b)$$

• TM-polarization ($\hat{z}$ polarization)

$$|(M_z)_{nm}^{\sigma}(k_t)|^2 = \frac{|<S|p_z|Z>|^2}{4} \cdot <\phi_n|g_m^{(3)}>^2 \qquad \text{for } \sigma=\text{U} \tag{2-16a}$$

$$|(M_z)_{nm}^{\sigma}(k_t)|^2 = \frac{|<S|p_z|Z>|^2}{4} \cdot <\phi_n|g_m^{(6)}>^2 \qquad \text{for } \sigma=\text{L} \tag{2-16b}$$

where ϕ_n and g_m are the conduction and valence band wave functions, respectively. The upper and lower Hamiltonian blocks are indicated by σ=U and σ=L, respectively. In our calculation, the linewidth broadening time (τ_s) is assumed to have Lorentzian shape with $\tau_s = 0.1ps$.

Based on the Fermi's Golden Rule, the spontaneous emission rate for TE (e=x) or TM (e=z) polarizations can be obtained by considering all the transitions between the n^{th} conduction subbands and m^{th} valence subbands as follows:

$$g_{sp}^{e}(\hbar\omega) = \frac{2q^2\pi}{n_r c\varepsilon_0 m_0^2 \omega L_\omega} \sum_{\sigma=U,L} \sum_{n,m} \int \frac{k_t dk_t}{2\pi} |(M_x)_{nm}^{\sigma}(k_t)|^2 \cdot \frac{f_n^c(k_t)(1-f_{\sigma m}^v(k_t))(\gamma/\pi)}{(E_{\sigma,nm}^{cv}(k_t)-\hbar\omega)^2+\gamma^2} \tag{2-17}$$

The optical gains for the TE (g^{TE}) and TM (g^{TM}) polarizations are related to the spontaneous emission rate as follows:

$$g^{TE}(\hbar\omega) = g_{sp}^{x}(\hbar\omega)[1-\exp(\frac{\hbar\omega-\Delta F}{k_B T})] \tag{2-18a}$$

$$g^{TM}(\hbar\omega) = g_{sp}^{z}(\hbar\omega)[1-\exp(\frac{\hbar\omega-\Delta F}{k_B T})] \tag{2-18b}$$

Note that the parameter ΔF is the separation of the quasi-Fermi levels of electrons (F_c) and the holes (F_v). The parameter ΔF can be expressed as $\Delta F = F_c - F_v$, which depends on the injection carrier densities (n and p) shown as follows:

$$n = \frac{2}{L_\omega} \sum_n \int \frac{k_t dk_t}{2\pi} f_n^c(k_t) \qquad (2\text{-}19)$$

$$p = \frac{1}{L_\omega} \sum_{\sigma=U,L} \sum_m \int \frac{k_t dk_t}{2\pi} (1 - f_{\sigma m}^v(k_t)) \qquad (2\text{-}20)$$

Note that $f_n^c(k_t)$ and $f_{\sigma m}^v(k_t)$ are the Fermi-Dirac distribution functions for the electrons in conduction band and valence band, given as follows:

$$f_n^c(k_t) = \frac{1}{1 + \exp(\frac{E_n^c(k_t) - F_c}{k_B T})} \qquad (2\text{-}21)$$

$$f_{\sigma m}^v(k_t) = \frac{1}{1 + \exp(\frac{E_{\sigma,m}^v(k_t) - F_v}{k_B T})} \qquad (2\text{-}22)$$

For the calculation of the spontaneous emission rate, we consider both TE and TM polarizations. The total momentum matrix element is the average of two TE-polarization components and one TM-polarization component [17], which can be expressed as follows:

$$|M_{sp}|^2 = \frac{1}{3}(2|M_x|^2 + |M_z|^2) \qquad (2\text{-}23)$$

The spontaneous emission rate ($s^{-1}cm^{-3}eV^{-1}$) can be written as follows:

$$r^{spon}(E = \hbar\omega) = \frac{n_e{}^2 \omega^2}{\pi^2 \hbar c^2} \frac{2(2g_{sp}^x + g_{sp}^z)}{3} \qquad (2\text{-}24)$$

The spontaneous emission radiative recombination rate ($s^{-1}cm^{-3}$) is obtained by integrating (2-24) over the entire frequency range as follows [22]:

$$R_{sp} = \int_0^{\infty} r^{spon}(\hbar\omega) d(\hbar\omega) \qquad (2\text{-}25)$$

2.4 Self-Consistent Schrödinger and Poisson Equations

The calculations of the eigenenergies and wave functions are based on the self-consistent model of solving the Poisson equation [22] expressed as follows:

$$\frac{\partial}{\partial z}(\varepsilon \frac{\partial V_{sc}}{\partial z}) = -\rho(z) \qquad (2\text{-}26)$$

where V_{sc} is an intermediate quantity and ρ(z) is the charge distribution given by:

$$\rho(z) = |e|[p(z) - n(z)] \qquad (2\text{-}27)$$

Note that the electron and hole concentrations are related to the wave functions of the nth conduction subband $\phi_n(z)$ and the mth valence subband $g_m(z)$. The corresponding surface electron concentration (N_n) and surface hole concentration (P_m) are given as follows:

$$n(z) = \sum_n |\phi_n(z)|^2 \, N_n \qquad (2\text{-}28)$$

$$p(z) = \sum_n |g_m(z)|^2 \, P_m \qquad (2\text{-}29)$$

The surface electron concentration in the n^{th} conduction band can be expressed as:

$$N_n = 2\int_0^{\infty} \frac{2\pi k_t}{(2\pi)^2} \frac{1}{1 + e^{[E_{en}(k_t) - F_c]/k_B T}} dk_t \qquad (2\text{-}30)$$

and the surface hole concentration in the m^{th} valence band is given by:

$$P_m = 2\int_0^{\infty} \frac{2\pi k_t}{(2\pi)^2} \frac{1}{1+e^{[-E_{hm}(k_t)+F_v]/k_BT}} dk_t \qquad (2\text{-}31)$$

The $V_{sc}(z)$ term will modify both the total potential profiles for electrons, $U_e(z)$, and holes, $U_h(z)$, as follows:

$$U_e(z) = U_0^e(z) - |e| V_{sc}(z) \qquad (2\text{-}32)$$

$$U_h(z) = U_0^h(z) - |e| V_{sc}(z) \qquad (2\text{-}33)$$

Thus, the self-consistent Schrödinger equations for the carrier screening effect of electrons and holes can be expressed as follows:

$$[-\frac{\hbar^2}{2m_e^*}\frac{d^2}{dz^2} + U_e(z)]\phi(z) = E_e\phi(z) \qquad (2\text{-}34)$$

$$[\frac{\hbar^2}{2m_h^*}\frac{d^2}{dz^2} + U_h(z)]g(z) = E_h g(z) \qquad (2\text{-}35)$$

Note that $V_{sc}(z)$, which is proportional to the carrier density *n*, is the dominant variable for the self-consistent process. Figure 2-1 reveals how $V_{sc}(z)$ changes with position z (nm) for carrier densities ranging from 1-6× $10^{19} cm^{-3}$ for the conventional 24-Å $In_{0.28}Ga_{0.72}N$ QW.

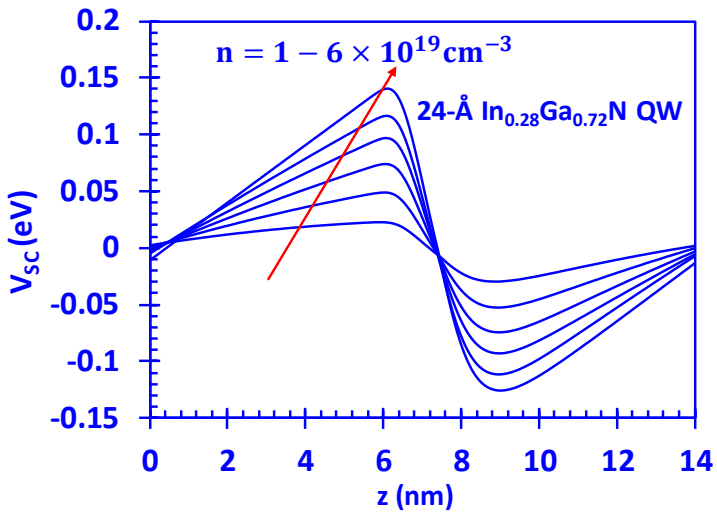

Figure 2-1: $V_{sc}(eV)$ versus position z (nm) for a conventional 24-Å $In_{0.28}Ga_{0.72}N$ QW. The carrier density n ranges from 1-6× $10^{19} cm^{-3}$.

2.5 Summary

In this chapter we have presented the Hamiltonian matrix elements, the spontaneous and piezoelectric polarization equations, momentum matrix elements, and self-consistent Schrödinger and Poisson equations based upon the 6-band $\boldsymbol{k \cdot p}$ formalism for wurtzite semiconductors. Under this formalism, we will utilize the finite difference method [23] to solve the band structures, spontaneous emission rates, and gain properties for InGaN-AlGaInN QWs in Chapters 3 and 4.

Chapter 3: Band Properties for InGaN-AlGaInN Quantum Wells

In Chapter 2, we have presented the 6-band ***k·p*** formalism for wurtzite semiconductors. In this chapter, we will present the band lineups, carrier concentration distributions, valence band structures, and momentum matrix elements characteristics for a conventional 24-Å $In_{0.28}Ga_{0.72}N$-GaN QW and strain-compensated 24-Å $In_{0.28}Ga_{0.72}N$-$Al_{0.2}Ga_{0.8}N$ QW, 24-Å $In_{0.28}Ga_{0.72}N$-$Al_{0.56}Ga_{0.32}In_{0.12}N$ QW, and 24-Å $In_{0.28}Ga_{0.72}N$-$Al_{0.78}Ga_{0.1}In_{0.12}N$ QW. We will analyze the difference among these QWs.

3.1 Band Lineups and Carrier Concentration Distributions

Band lineups and carrier concentration distributions are crucial properties for the study of quantum well structures. In figure 3-1, we present the self-consistent band lineups and carrier concentration distributions of 24-Å $In_{0.28}Ga_{0.72}N$-GaN QW [Fig.3-1(a)], 24-Å $In_{0.28}Ga_{0.72}N$-$Al_{0.2}Ga_{0.8}N$ QW[Fig.3-1(b)], 24-Å $In_{0.28}Ga_{0.72}N$-$Al_{0.56}Ga_{0.32}In_{0.12}N$ QW [Fig.3-1(c)], and 24-Å $In_{0.28}Ga_{0.72}N$- $Al_{0.78}Ga_{0.1}In_{0.12}N$ QW [Fig.3-1(d)] for the carrier density n=6× $10^{19}cm^{-3}$.

First, figure 3-1 illustrates that the slope of the lineups (electric field) for both conventional and strain-compensated QWs become more flattened after the self-consistent process. This is due to a broader distribution of carrier concentration which reduces the magnitude of peak concentration after the self-consistent Schrödinger and Poisson process.

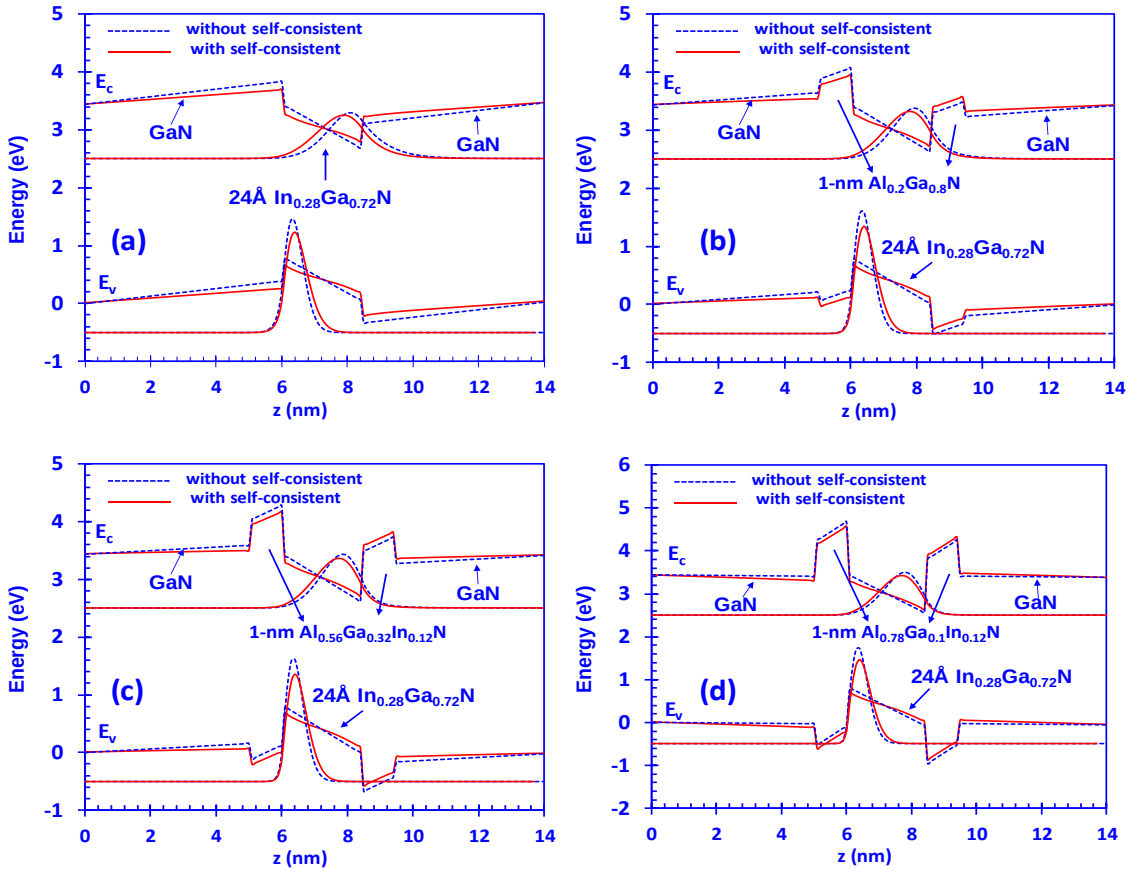

Figure 3-1: Self-consistent band lineups and carrier concentration distributions of (a) 24-Å $In_{0.28}Ga_{0.72}N$-GaN QW, (b) 24-Å $In_{0.28}Ga_{0.72}N$-$Al_{0.2}Ga_{0.8}N$ QW, (c) 24-Å $In_{0.28}Ga_{0.72}N$-$Al_{0.56}Ga_{0.32}In_{0.12}N$ QW, and (d) 24-Å $In_{0.28}Ga_{0.72}N$-$Al_{0.78}Ga_{0.1}In_{0.12}N$ QW for carrier density n=6× $10^{19}cm^{-3}$.

Second, figure 3-1 illustrates that for both conventional and strain-compensated QWs, the hole concentration distributions are narrower than the electron concentration distributions. This is because the concentration is proportional to the wave function distribution, which is calculated by the Schrödinger equation. We know that the electron effective mass is much smaller than the hole effective mass, so the wave function distribution calculated by the Schrödinger equation for electrons will appear broader than that of the holes.

Third, compared to the conventional QW, the strain-compensated QWs have a higher confinement potential for InGaN QW. This improved confinement results in better optical properties. We will detail the analysis in Chapter 4.

3.2 Valence Band Structures

The valence band structures of both the conventional InGaN–GaN QW and the strain-compensated QWs are calculated from (2-2) - (2-14), using the parameters of GaN, InN, and AlN shown in table 3-1 [21]. The bowing parameters used to calculate the bandgaps for InGaN, AlGaN and AlInN are 1.4 eV, 0.8 eV and 2.74 eV, respectively. Other parameters for AlGaInN use linear interpolation of the binary alloy (InN, GaN, AlN) parameters.

In figure 3-2, the shape of the band-edge structures for both conventional and the strain-compensated QWs are very similar, which suggests they have similar effective masses. However, there are some important differences to emphasize.

First, compared to the conventional QW, the HH1 and LH1 subbands of the strain-compensated QWs shift up about 0.02eV (b), 0.01ev (c) and 0.015eV (d), respectively.

Second, the separations of the subband energy levels (HH1, LH1 & HH2, LH2) increases in general, as the barrier bandgap increases. This can be attributed to the stronger quantum confinement effect from the larger band offsets between the barrier and QW in the case of strain-compensated InGaN-AlGaInN system.

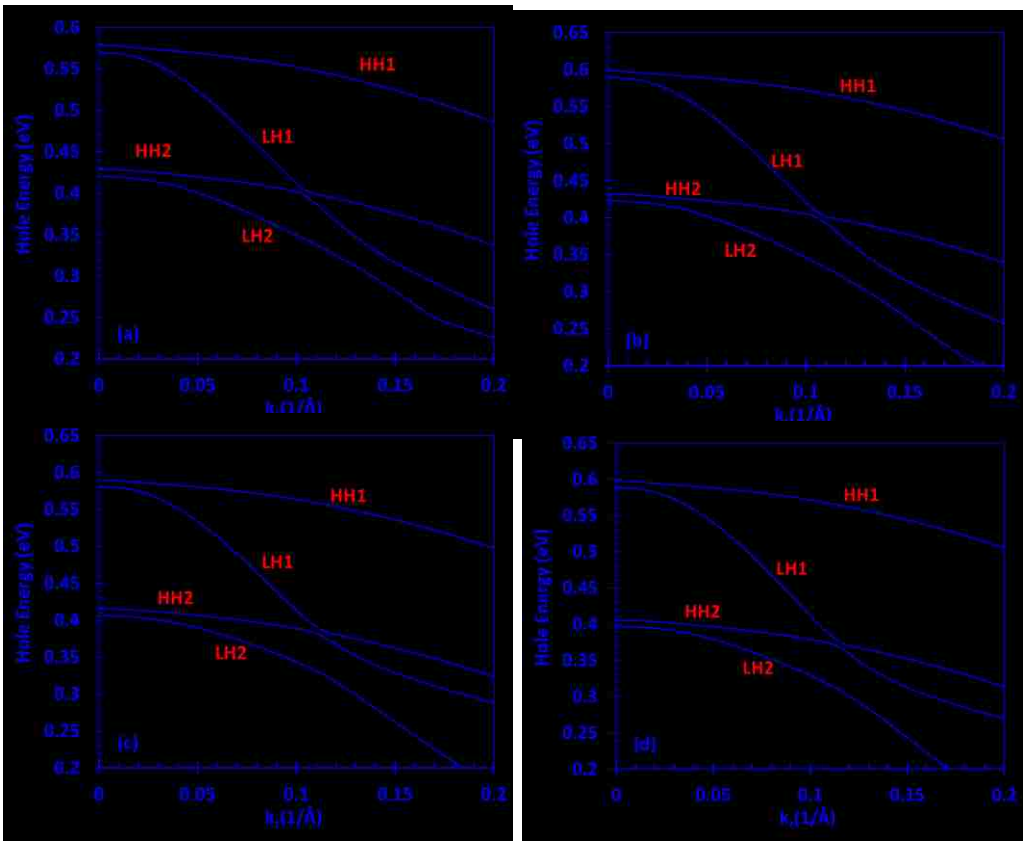

Figure 3-2: Valence band structures for the (a) 24-Å $In_{0.28}Ga_{0.72}N$-GaN QW (b) 24-Å $In_{0.28}Ga_{0.72}N$-$Al_{0.2}Ga_{0.8}N$ QW, (c) 24-Å $In_{0.28}Ga_{0.72}N$-$Al_{0.56}Ga_{0.32}In_{0.12}N$ QW, and (d) 24-Å $In_{0.28}Ga_{0.72}N$-$Al_{0.78}Ga_{0.1}In_{0.12}N$ QW for the carrier density n=6× $10^{19}cm^{-3}$..

Finally, note that the valence subbands will not cross one another. Whenever they trend to a crossing, the two subbands seem to repel away from one another and exchange their wave functions. This phenomenon is called valence band mixing.

Parameters	GaN	AlN	InN
Lattice constant (Å)			
a	3.189	3.112	3.545
c	5.185	4.982	5.703
Energy Parameters			
E_g (eV) at 300 K	3.437	6.00	0.6405
$\Delta_1(=\Delta_{cr})$ (eV)	0.010	-0.227	0.024
$\Delta_1=\Delta_2=\Delta_{so}/3$ (eV)	0.00567	0.012	0.00167
Conduction-band effective masses			
$m_{//}^*/m_0$ at 300K	0.21	0.32	0.07
$m_{\perp}^*/m_0$ at 300K	0.20	0.30	0.07
Valence-band effective mass parameters			
A_1	-7.21	-3.86	-8.21
A_2	-0.44	-0.25	-0.68
A_3	6.68	.58	7.57
A_4	-3.46	-1.32	-5.23
A_5	-3.40	-1.47	-5.11
A_6	-4.90	-1.64	-5.96
Deformation potentials (eV)			
a_{cz} (eV)	-7.1	-3.4	-4.2
a_{ct} (eV)	-9.9	-11.8	-4.2
D_1 (eV)	-3.6	-2.9	-3.6
D_2 (eV)	1.7	4.9	1.7
D_3 (eV)	5.2	9.4	5.2
D_4 (eV)	-2.7	-4.0	-2.7
Elastic stiffness constants			
C_{11} (GPa)	390	396	223
C_{12} (GPa)	145	137	115
C_{13} (GPa)	106	108	92
C_{33} (GPa)	398	373	224
Piezoelectric coefficients			
d_{13} (pmV^{-1})	-1.0	-2.1	-3.5
d_{33} (pmV^{-1})	1.9	5.4	7.6
Spontaneous Polarization			
P_{sp} (C/m^2)	-0.034	-0.090	-0.042

Table 3-1: Material parameters for GaN, AlN, and InN. The values are taken from [21].

3.3 Momentum Matrix Elements Characteristics

The momentum matrix elements describe the optical transitions between the n^{th}-state in conduction band and m^{th}-state in valence band. The equations (2-15) and (2-16) in Chapter 2 describe the momentum matrix elements for TE polarization and TM polarization, respectively.

Figure 3-3 shows the square value of the momentum matrix element as a function of the wave vector k_t in the TE-polarization for 24-Å $In_{0.28}Ga_{0.72}N$-GaN QW [Fig.3-3(a)], 24-Å $In_{0.28}Ga_{0.72}N$-$Al_{0.2}Ga_{0.8}N$ QW [Fig.3-3(b)], 24-Å $In_{0.28}Ga_{0.72}N$-$Al_{0.56}Ga_{0.32}In_{0.12}N$ QW [Fig.3-3(c)], and 24-Å $In_{0.28}Ga_{0.72}N$-$Al_{0.78}Ga_{0.1}In_{0.12}N$ QW [Fig.3-3(d)] for the carrier density of n=3× $10^{19}cm^{-3}$.

Figure 3-3 illustrates that for both the conventional and strain-compensated QWs, the transitions between C1-HH1, C1-LH1, C1-HH2, and C1-LH2 are fairly strong. These transitions are major contributions to the spontaneous emission rate. However, the transitions between C2-

HH1, C2-LH1, C2-HH2, and C2-LH2 are much weaker. This fact indicates that their contributions for the spontaneous emission rate are minor.

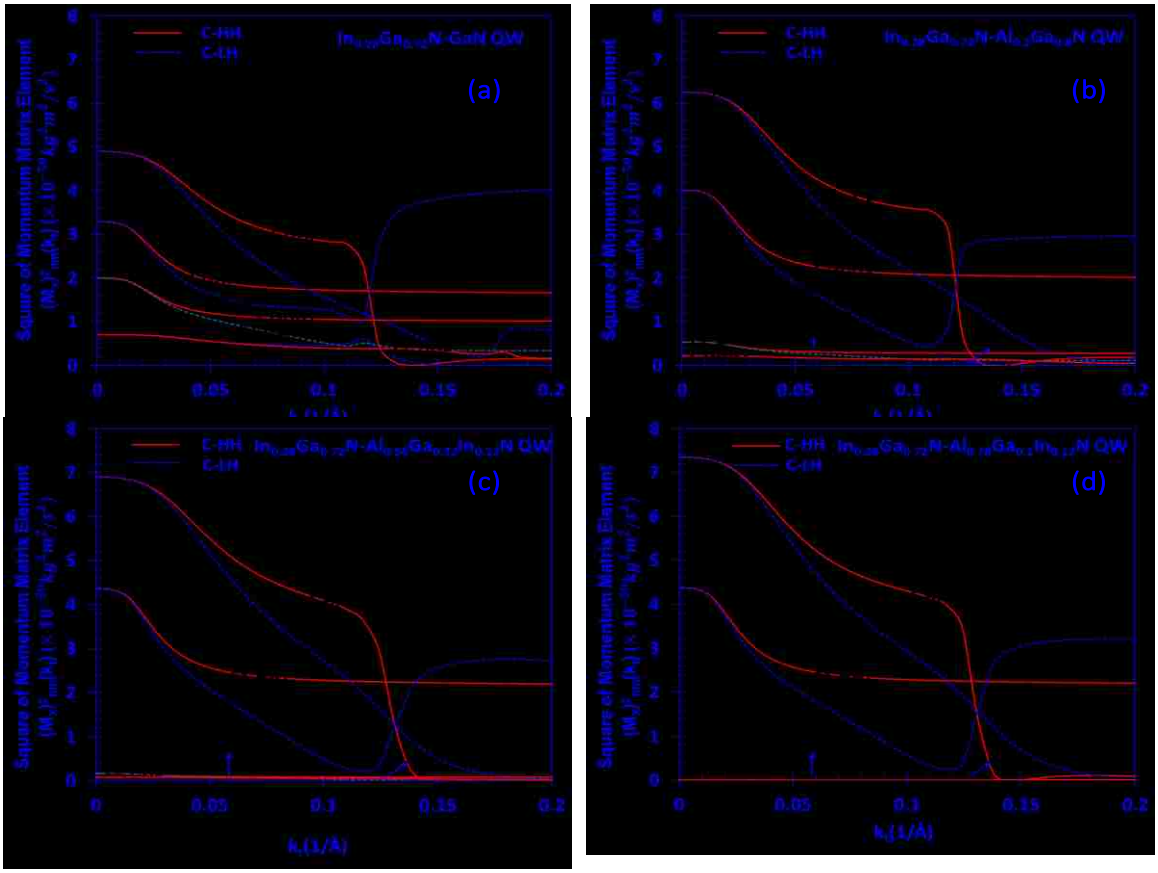

Figure 3-3: Square value of momentum matrix elements as a function of the wave vector k_t in the TE-polarization for the (a) 24-Å $In_{0.28}Ga_{0.72}N$-GaN QW (b) 24-Å $In_{0.28}Ga_{0.72}N$-$Al_{0.2}Ga_{0.8}N$ QW, (c) 24-Å $In_{0.28}Ga_{0.72}N$-$Al_{0.56}Ga_{0.32}In_{0.12}N$ QW, and (d) 24-Å $In_{0.28}Ga_{0.72}N$-$Al_{0.78}Ga_{0.1}In_{0.12}N$ QW for the carrier density n=3× $10^{19}cm^{-3}$

Compared to the conventional QW, the transitions between C1-HH1, C1-LH1, C1-HH2, and C1-LH2 get larger while the transitions between C2-HH1, C2-LH1, C2-HH2, and C2-LH2 become smaller with the increasing of the barrier bandgap. The increasing barrier bandgap offers better confinement for carriers which results in larger conduction and valence wave function overlaps between C1-HH1, C1-LH1, C1-HH2, and C1-LH2 transitions. Meanwhile, the conduction and

valence band overlaps for C2-HH1, C2-LH1, C2-HH2, and C2-LH2 reduce because the band dispersion gets larger as the barrier bandgap increases (explained in Section 3.2).

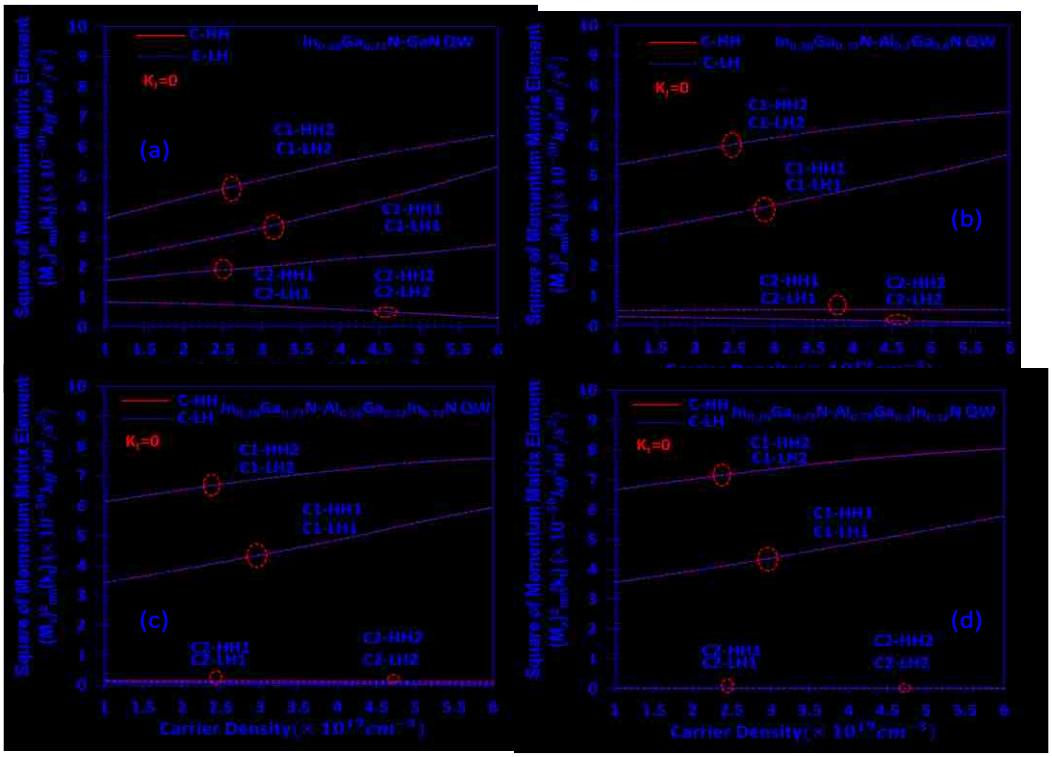

Figure 3-4: Square value of momentum matrix elements at zone center (k_t=0) using the self-consistent model as a function of the carrier density for the (a) 24-Å $In_{0.28}Ga_{0.72}N$-GaN QW (b) 24-Å $In_{0.28}Ga_{0.72}N$-$Al_{0.2}Ga_{0.8}N$ QW, (c) 24-Å $In_{0.28}Ga_{0.72}N$-$Al_{0.56}Ga_{0.32}In_{0.12}N$ QW, and (d) 24-Å $In_{0.28}Ga_{0.72}N$-$Al_{0.78}Ga_{0.1}In_{0.12}N$ QW.

Another characteristic of the momentum matrix elements is shown in figure 3-4. We plot the square value of the momentum matrix elements at the zone center (k_t=0) using the self-consistent model as a function of the carrier density for 24-Å $In_{0.28}Ga_{0.72}N$-GaN QW [Fig.3-4(a)], 24-Å $In_{0.28}Ga_{0.72}N$- $Al_{0.2}Ga_{0.8}N$ QW [Fig.3-4(b)], 24-Å $In_{0.28}Ga_{0.72}N$-$Al_{0.56}Ga_{0.32}In_{0.12}N$ QW [Fig.3-4(c)], and 24-Å $In_{0.28}Ga_{0.72}N$-$Al_{0.78}Ga_{0.1}In_{0.12}N$ QW [Fig.3-4(d)].

Figure 3-4 illustrates that both the conventional and strain-compensated QWs indicate an increasing value of the momentum matrix elements with increasing carrier density for transitions between C1-HH1, C1-LH1, C1-HH2, and C1-LH2.

Compared to the conventional QW, the square value of the momentum matrix elements for the C1-HH1, C1-LH1, C1-HH2, and C1-LH2 transitions gets larger with increasing barrier bandgap for strain-compensated QWs. Increasing the barrier bandgap results in better confinement in the QWs, which increases the conduction band and valence band wave function overlaps. We know from figure 3-4 that as the carrier density increases, the square value of the momentum matrix elements of C2-HH1, C2-LH1, C2-HH2, and C2-LH2 becomes negligible.

3.4 Summary

We present comprehensive analysis of band lineups, carrier concentration distributions, valence band structures, and momentum matrix elements characteristics for the conventional 24-Å $In_{0.28}Ga_{0.72}N$-GaN QW and strain-compensated 24-Å $In_{0.28}Ga_{0.72}N$-$Al_{0.2}Ga_{0.8}N$ QW, 24-Å $In_{0.28}Ga_{0.72}N$-$Al_{0.56}Ga_{0.32}In_{0.12}N$ QW, and 24-Å $In_{0.28}Ga_{0.72}N$-$Al_{0.78}Ga_{0.1}In_{0.12}N$ QW in this chapter. We have compared and explained the differences in band properties between conventional and strain-compensated QWs in this chapter.

Chapter 4: Optical Properties of InGaN-AlGaInN Quantum Wells

The optical properties, such as spontaneous emission and gain characteristics, are key metrics for active region design in LEDs and lasers devices. We have presented a thorough analysis of the band properties for conventional and strain-compensated QWs in Chapter 3. In this chapter, we will discuss the spontaneous emission spectra and gain properties for conventional and strain-compensated QWs.

4.1 Spontaneous Emission Characteristics

Based on the self-consistent 6-band ***k·p*** formalism discussed in Chapter 2, we calculate the spontaneous emission spectra for 24-Å $In_{0.28}Ga_{0.72}N$-GaN QW , 24-Å $In_{0.28}Ga_{0.72}N$-$Al_{0.2}Ga_{0.8}N$ QW ,24-Å $In_{0.28}Ga_{0.72}N$-$Al_{0.56}Ga_{0.32}In_{0.12}N$ QW, and 24-Å $In_{0.28}Ga_{0.72}N$-$Al_{0.78}Ga_{0.1}In_{0.12}N$ QW, with carrier densities ranging from n=5$\times 10^{18}cm^{-3}$ up to n=6$\times 10^{19}cm^{-3}$ at T=300K. We plot the strain-compensated QWs (red solid line) with conventional QW (blue dotted line) in each figure for comparison. We divide this into two figures, Fig.4-1 and Fig.4-2, with carrier densities ranging from n=5$\times 10^{18}cm^{-3}$ up to n=10$\times 10^{18}cm^{-3}$ and n=2$\times 10^{19}cm^{-3}$ up to n=6$\times 10^{19}cm^{-3}$, respectively.

Figure 4-1 illustrates that the spontaneous emission rate for the strain-compensated QWs is much larger compared to the conventional QW in the low carrier density regime. The enhancements of the spontaneous emission rate for 24-Å $In_{0.28}Ga_{0.72}N$-$Al_{0.2}Ga_{0.8}N$ QW, 24-Å $In_{0.28}Ga_{0.72}N$-$Al_{0.56}Ga_{0.32}In_{0.12}N$ QW, and 24-Å $In_{0.28}Ga_{0.72}N$-$Al_{0.78}Ga_{0.1}In_{0.12}N$ QW for the carrier density n=10$\times 10^{18}cm^{-3}$are 44.4%, 66.7%, and 61.1%, respectively.

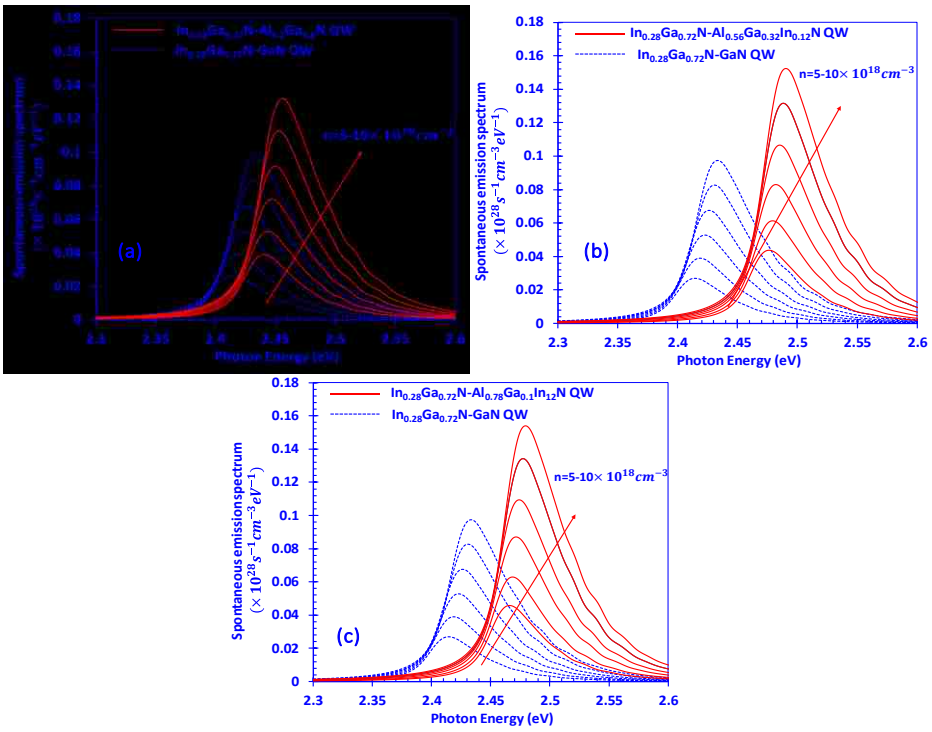

Figure 4-1: Spontaneous emission spectra comparison of (a) 24-Å $In_{0.28}Ga_{0.72}N$-$Al_{0.2}Ga_{0.8}N$ QW and conventional 24-Å $In_{0.28}Ga_{0.72}N$-GaN QW (b) 24-Å $In_{0.28}Ga_{0.72}N$-$Al_{0.56}Ga_{0.32}In_{0.12}N$ QW and conventional 24-Å $In_{0.28}Ga_{0.72}N$-GaN QW (c) 24-Å $In_{0.28}Ga_{0.72}N$-$Al_{0.78}Ga_{0.1}In_{0.12}N$ QW and conventional 24-Å $In_{0.28}Ga_{0.72}N$-GaN QW. The carrier densities range from n=5× $10^{18}cm^{-3}$ up to n=10× $10^{18}cm^{-3}$.

Figure 4-2 demonstrates that the spontaneous emission rate for strain-compensated QWs is larger than that of the conventional QW in the high carrier density regime. However, the percentage of enhancement is less than that in the low carrier density range. The enhancements of the spontaneous emission rate for 24-Å $In_{0.28}Ga_{0.72}N$-$Al_{0.2}Ga_{0.8}N$ QW, 24-Å $In_{0.28}Ga_{0.72}N$-$Al_{0.56}Ga_{0.32}In_{0.12}N$ QW, and 24-Å $In_{0.28}Ga_{0.72}N$-$Al_{0.78}Ga_{0.1}In_{0.12}N$ QW n=6 × $10^{19}cm^{-3}$ are 6.8%, 14.1%, and 8.2%, respectively.

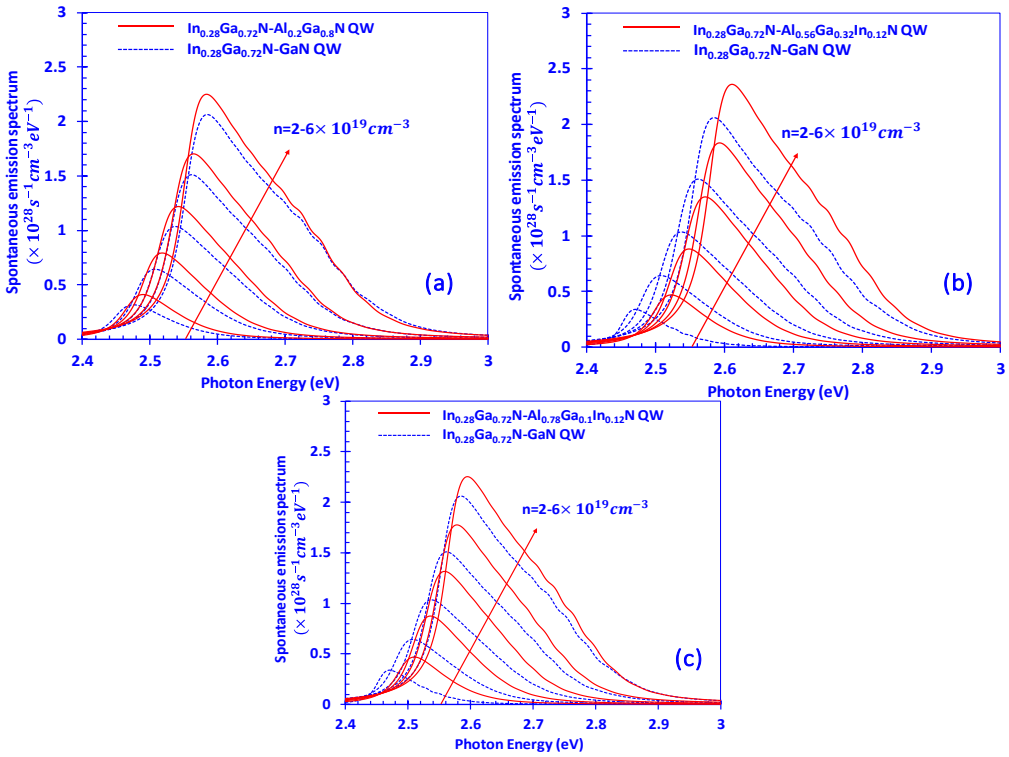

Figure 4-2: Spontaneous emission spectra comparison of (a) 24-Å $In_{0.28}Ga_{0.72}N$-$Al_{0.2}Ga_{0.8}N$ QW and conventional 24-Å $In_{0.28}Ga_{0.72}N$-GaN QW (b) 24-Å $In_{0.28}Ga_{0.72}N$-$Al_{0.56}Ga_{0.32}In_{0.12}N$ QW and conventional 24-Å $In_{0.28}Ga_{0.72}N$-GaN QW (c) 24-Å $In_{0.28}Ga_{0.72}N$-$Al_{0.78}Ga_{0.1}In_{0.12}N$ QW and conventional 24-Å $In_{0.28}Ga_{0.72}N$-GaN QW. The carrier densities range from n=2× $10^{19}cm^{-3}$ up to n=6× $10^{19}cm^{-3}$.

From both figures 4-1 and 4-2, we observe a blue shift in strain-compensated 24-Å $In_{0.28}Ga_{0.72}N$-$Al_{0.2}Ga_{0.8}N$ QW, 24-Å $In_{0.28}Ga_{0.72}N$-$Al_{0.56}Ga_{0.32}In_{0.12}N$ QW, and 24-Å $In_{0.28}Ga_{0.72}N$-$Al_{0.78}Ga_{0.1}In_{0.12}N$ QW compared to the conventional QW. This is due to the larger band dispersion from the increased barrier bandgap, as discussed in Section 3.2.

For laser operation, the typical threshold carrier density of InGaN QW ranges from $n = 3.5 \times 10^{19}cm^{-3}$ to $n = 7 \times 10^{19}cm^{-3}$ [24]. For the case of $n = 3 \times 10^{19}cm^{-3}$ ($n = 5 \times$

$10^{19}cm^{-3}$), the strain-compensated InGaN QW structures exhibit enhancement factors as given in table 4-1.

	GaN	$Al_{0.2}Ga_{0.8}N$	$Al_{0.56}Ga_{0.32}In_{0.12}N$	$Al_{0.78}Ga_{0.1}In_{0.12}N$
Lattice constant (Å)	3.1890	3.1736	3.1886	3.1717
Bandgap (eV)	3.437	3.822	4.156	4.765
Enhancement factor (n=3× $10^{19}cm^{-3}$)	100%	122%	135%	132%
Enhancement factor (n=5× $10^{19}cm^{-3}$)	100%	112%	119%	116%

Table 4-1: Enhancement factors of the spontaneous emission rate for strain-compensated 24-Å $In_{0.28}Ga_{0.72}N$- $Al_{0.2}Ga_{0.8}N$ QW, 24-Å $In_{0.28}Ga_{0.72}N$-$Al_{0.56}Ga_{0.32}In_{0.12}N$ QW, and 24-Å $In_{0.28}Ga_{0.72}N$-$Al_{0.78}Ga_{0.1}In_{0.12}N$ QW compared to conventional 24-Å $In_{0.28}Ga_{0.72}N$-GaN QW at transparency(n=3× $10^{19}cm^{-3}$) and near threshold (n=5× $10^{19}cm^{-3}$).

In figure 4-3, we plot the peak value of spontaneous emission rate versus increasing barrier bandgap (eV) for 24-Å $In_{0.28}Ga_{0.72}N$-GaN (3.437eV) QW, 24-Å $In_{0.28}Ga_{0.72}N$- $Al_{0.2}Ga_{0.8}N$ (3.822eV) QW, 24-Å $In_{0.28}Ga_{0.72}N$-$Al_{0.56}Ga_{0.32}In_{0.12}N$ (4.156 eV) QW, 24-Å $In_{0.28}Ga_{0.72}N$-$Al_{0.72}Ga_{0.13}In_{0.15}N$ (4.465eV) QW, 24-Å $In_{0.28}Ga_{0.72}N$-$Al_{0.78}Ga_{0.1}In_{0.12}N$ (4.765eV) QW, and 24-Å $In_{0.28}Ga_{0.72}N$-$Al_{0.82}Ga_{0.1}In_{0.08}N$ (5.065eV) QW. The carrier density is calculated at n=6× $10^{19}cm^{-3}$. The figure shows a parabolic shape for barrier bandgaps from 3.43eV-5.06eV, which indicates that one can obtain an optimized 1-nm strain compensated barrier for 24-Å $In_{0.28}Ga_{0.72}N$-AlGaInN QW between bandgaps of 4.2eV and 4.4eV which provides best spontaneous emission properties. Note that the figure is plotted for a carrier density n=6× $10^{19}cm^{-3}$ only for illustrative purposes.

In fact, we get similar results for all calculated carrier densities ranging from n=1 × $10^{18}cm^{-3}$ up to $\mathrm{n} = 6 \times 10^{19}cm^{-3}$.

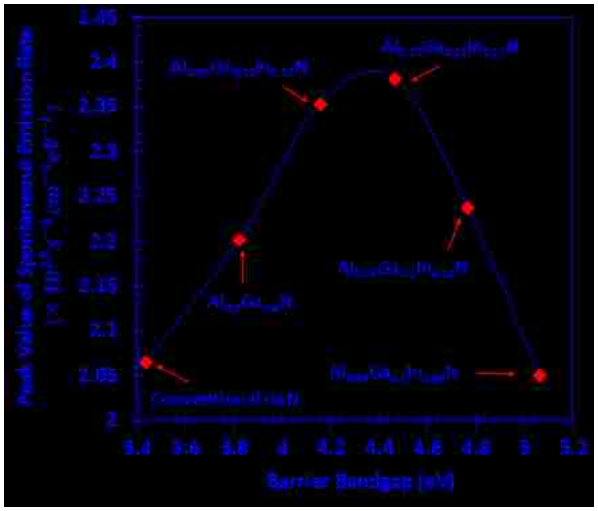

Figure 4-3: Peak value of spontaneous emission rate versus increasing barrier bandgap (eV) for 24-Å $In_{0.28}Ga_{0.72}N$-GaN QW (3.437eV), 24-Å $In_{0.28}Ga_{0.72}N$-$Al_{0.2}Ga_{0.8}N$ QW (3.822eV), 24-Å $In_{0.28}Ga_{0.72}N$-$Al_{0.56}Ga_{0.32}In_{0.12}N$ QW (4.156eV), 24-Å $In_{0.28}Ga_{0.72}N$-$Al_{0.72}Ga_{0.13}In_{0.15}N$ QW (4.465eV), 24-Å $In_{0.28}Ga_{0.72}N$-$Al_{0.78}Ga_{0.1}In_{0.12}N$ QW (4.765eV), and 24-Å $In_{0.28}Ga_{0.72}N$-$Al_{0.82}Ga_{0.1}In_{0.08}N$ QW (5.065eV). The carrier density is calculated at n=6× $10^{19}cm^{-3}$.

In figure 4-4, the spontaneous emission radiative recombination rate (R_{SP}) of the strain-compensated $In_{0.28}Ga_{0.72}N$–$Al_{0.2}Ga_{0.8}N$ QW, $In_{0.28}Ga_{0.72}N$–$Al_{0.56}Ga_{0.32}In_{0.12}N$ QW, and $In_{0.28}Ga_{0.72}N$–$Al_{0.78}Ga_{0.1}In_{0.12}N$ QW and conventional $In_{0.28}Ga_{0.72}N$–GaN QW are plotted against carrier density (n), in the low carrier density regime (from $n = 1 \times 10^{18}cm^{-3}$ up to $n = 10 \times 10^{18}cm^{-3}$) [Fig.5-4(a)] and the high carrier density regime (from $n = 2 \times 10^{19}cm^{-3}$ up to $n = 6 \times 10^{19}cm^{-3}$) [Fig.5-4(b)], respectively. The spontaneous emission radiative recombination rate can be obtained from (2-25).

Figure 4-4 illustrates that the spontaneous emission radiative recombination rate for strain-compensated QWs is much higher compared to the conventional QW in the low carrier

density regime. However, the enhancement of the spontaneous emission radiative recombination rate in the higher carrier density regime is not as significant as in the lower regime.

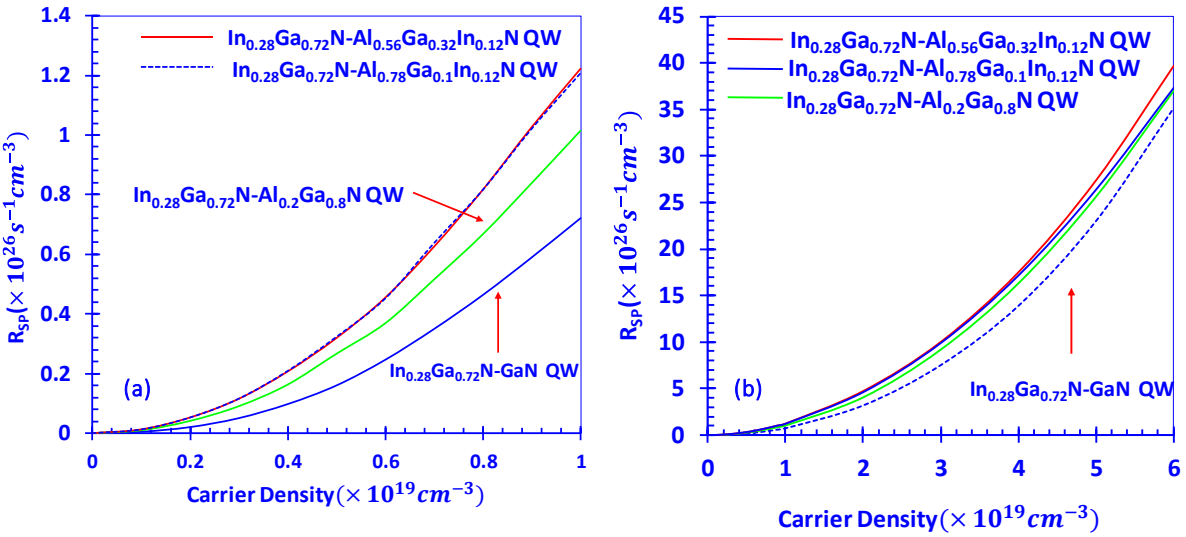

Figure 4-4: Spontaneous emission radiative recombination rate comparison as a function of carrier density at 300K for 24-Å $In_{0.28}Ga_{0.72}N$-$Al_{0.2}Ga_{0.8}N$ QW, 24-Å $In_{0.28}Ga_{0.72}N$-$Al_{0.56}Ga_{0.32}In_{0.12}N$ QW, 24-Å $In_{0.28}Ga_{0.72}N$-$Al_{0.78}Ga_{0.1}In_{0.12}N$ QW, and 24-Å $In_{0.28}Ga_{0.72}N$-GaN QW. The carrier densities range from (a) n=1× $10^{18}cm^{-3}$ up to n=10× $10^{18}cm^{-3}$ and (b) n=1× $10^{18}cm^{-3}$ up to n=6× $10^{19}cm^{-3}$.

In figure 4-5, we show the ratio of the spontaneous emission radiative recombination rate (R_{SP}) for strain-compensated InGaN-AlGaInN QWs and the conventional InGaN QW as a function of carrier density at 300K for carrier densities $n = 1 \times 10^{18}cm^{-3}$ up to $n = 6 \times 10^{19}cm^{-3}$.

The figure 4-5 indicates a large enhancement factor of about 60%-180% in strain-compensated QWs in the low carrier regime. The enhancement factor is decreasing as the carrier density increases.

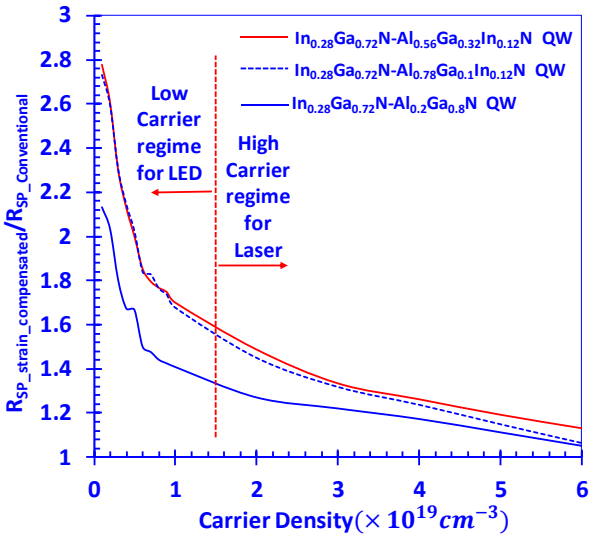

Figure 4-5: Ratio of spontaneous emission radiative recombination rate (R_{SP}) for strain compensated 24-Å $In_{0.28}Ga_{0.72}N$-$Al_{0.2}Ga_{0.8}N$ QW, 24-Å $In_{0.28}Ga_{0.72}N$-$Al_{0.56}Ga_{0.32}In_{0.12}N$ QW, 24-Å $In_{0.28}Ga_{0.72}N$-$Al_{0.78}Ga_{0.1}In_{0.12}N$ QW, and conventional 24-Å $In_{0.28}Ga_{0.72}N$-GaN QW as function of carrier density at temperature of 300K. The ratio is plotted from n=$1\times 10^{18} cm^{-3}$ up to n=$6\times 10^{19} cm^{-3}$.

4.2 Optical Gain Characteristics

Based on the self-consistent 6-band $\boldsymbol{k\cdot p}$ formalism discussed in Chapter 2, we can calculate the gain properties for both conventional and strain-compensated QWs by (2-18a) and (2-18b). Note that the TM-polarized optical gain is negligible for the case of compressively strained InGaN QW [17], so the optical gain is almost completely TE-polarized.

In figure 4-6, the optical TE-polarized optical gain spectra of strain-compensated 24-Å $In_{0.28}Ga_{0.72}N$-$Al_{0.2}Ga_{0.8}N$ QW [Fig.4-6(a)], 24-Å $In_{0.28}Ga_{0.72}N$-$Al_{0.56}Ga_{0.32}In_{0.12}N$ QW [Fig.4-6(b)], and 24-Å $In_{0.28}Ga_{0.72}N$-$Al_{0.78}Ga_{0.1}In_{0.12}N$ QW [Fig.4-6(c)] compared to conventional 24-Å $In_{0.28}Ga_{0.72}N$-GaN QW are plotted for carrier densities (n) from n=$3\times 10^{19} cm^{-3}$ up to n=$6\times 10^{19} cm^{-3}$.

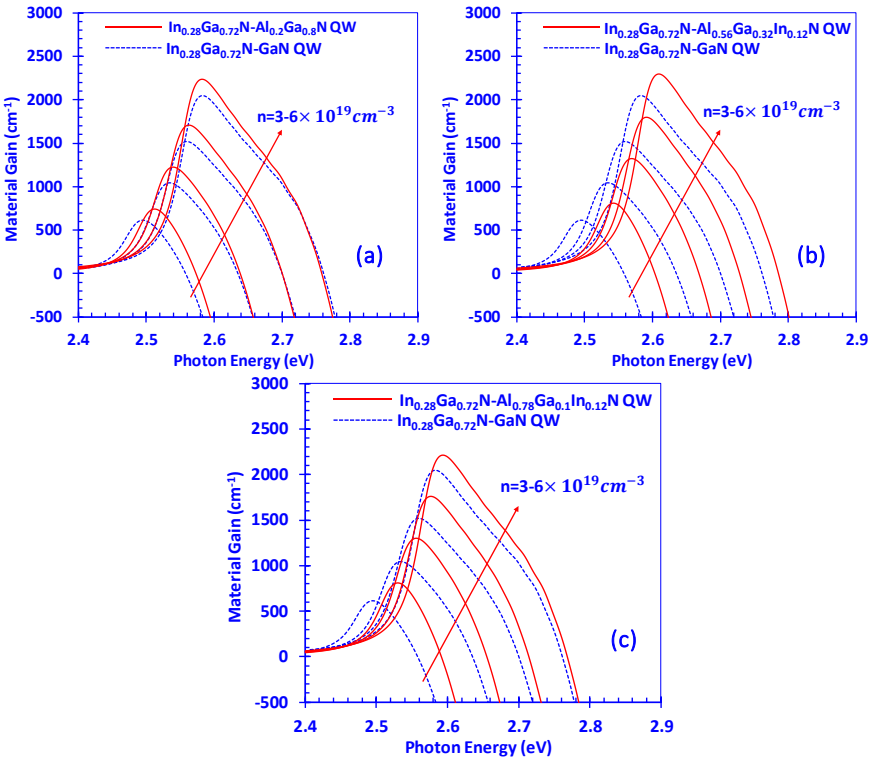

Figure 4-6: TE-polarized optical gain spectra of strain-compensated 24-Å $In_{0.28}Ga_{0.72}N$-$Al_{0.2}Ga_{0.8}N$ QW (a), 24-Å $In_{0.28}Ga_{0.72}N$-$Al_{0.56}Ga_{0.32}In_{0.12}N$ QW (b), and 24-Å $In_{0.28}Ga_{0.72}N$-$Al_{0.78}Ga_{0.1}In_{0.12}N$ QW (c) compared to the conventional 24-Å $In_{0.28}Ga_{0.72}N$-GaN QW for carrier density (n) from n=3× $10^{19}cm^{-3}$ up to n=6× $10^{19}cm^{-3}$.

Figure 4-6 illustrates that the optical gain for strain-compensated QWs is larger than in conventional QWs. For example, in the relatively high carrier density $n = 5 \times 10^{19}cm^{-3}$(near threshold condition), the peak optical gain of the strain-compensated $In_{0.28}Ga_{0.72}N$–$Al_{0.2}Ga_{0.8}N$ QW, $In_{0.28}Ga_{0.72}N$–$Al_{0.56}Ga_{0.32}In_{0.12}N$ QW, and $In_{0.28}Ga_{0.72}N$–$Al_{0.78}Ga_{0.1}In_{0.12}N$ QW structure exhibit peak material gain (g_p) of 1731.9 cm^{-1}, 1799.5 cm^{-1} , and 1763.0 cm^{-1} , which correspond to improvements of 12.2%, 16.6%, and 14.2%, respectively, in comparison to the conventional $In_{0.28}Ga_{0.72}N$–GaN QW structure (g_p=1543.5 cm^{-1} at $n = 5 \times 10^{19}cm^{-3}$) (Table 4-2).

	GaN	$Al_{0.2}Ga_{0.8}N$	$Al_{0.56}Ga_{0.32}In_{0.12}N$	$Al_{0.78}Ga_{0.1}In_{0.12}N$
Lattice constant (Å)	3.1890	3.1736	3.1886	3.1717
Bandgap (eV)	3.437	3.822	4.156	4.765
Gain (n=5× $10^{19}cm^{-3}$)	1543.5	1731.9	1799.3	1763.0
Enhancement factor (n=5× $10^{19}cm^{-3}$)	100%	112.2%	116.6%	114.2%

Table 4-2: Material gain and enhancement factors for 24-Å $In_{0.28}Ga_{0.72}N$-$Al_{0.2}Ga_{0.8}N$ QW, 24-Å $In_{0.28}Ga_{0.72}N$-$Al_{0.56}Ga_{0.32}In_{0.12}N$ QW, and 24-Å $In_{0.28}Ga_{0.72}N$-$Al_{0.78}Ga_{0.1}In_{0.12}N$ QW compared to conventional 24-Å $In_{0.28}Ga_{0.72}N$-GaN QW near threshold (n=5× $10^{19}cm^{-3}$).

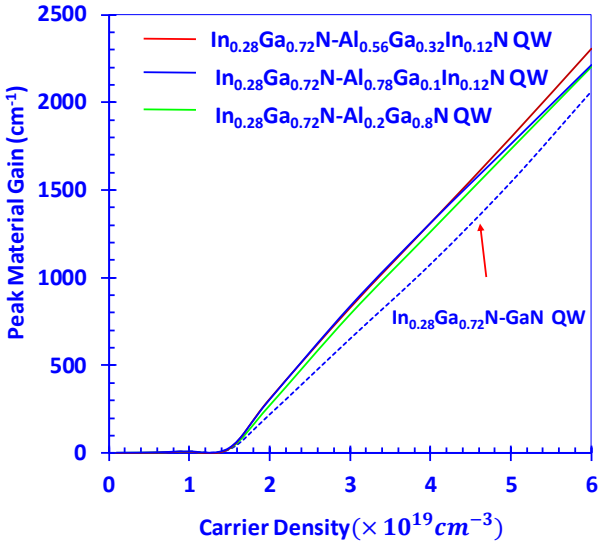

Figure 4-7: Peak material gain as a function of carrier density at 300 K for 24-Å $In_{0.28}Ga_{0.72}N$-$Al_{0.2}Ga_{0.8}N$ QW, 24-Å $In_{0.28}Ga_{0.72}N$-$Al_{0.56}Ga_{0.32}In_{0.12}N$ QW, 24-Å $In_{0.28}Ga_{0.72}N$-$Al_{0.78}Ga_{0.1}In_{0.12}N$ QW, and 24-Å $In_{0.28}Ga_{0.72}N$-GaN QW for carrier densities range from n=1× $10^{18}cm^{-3}$ up to n=6× $10^{19}cm^{-3}$.

To reveal another aspect of the optical gain properties, we plot the peak material gain versus carrier density for the strain-compensated QWs and the conventional QW in figure 4-7.

From figure 4-7, we can conclude that the transparency carrier density is n_{tr}~$1.5 \times 10^{19} cm^{-3}$. The peak material gain increases almost linearly with the carrier density after transparency. The peak material gain of strain-compensated QWs is larger than the conventional QW.

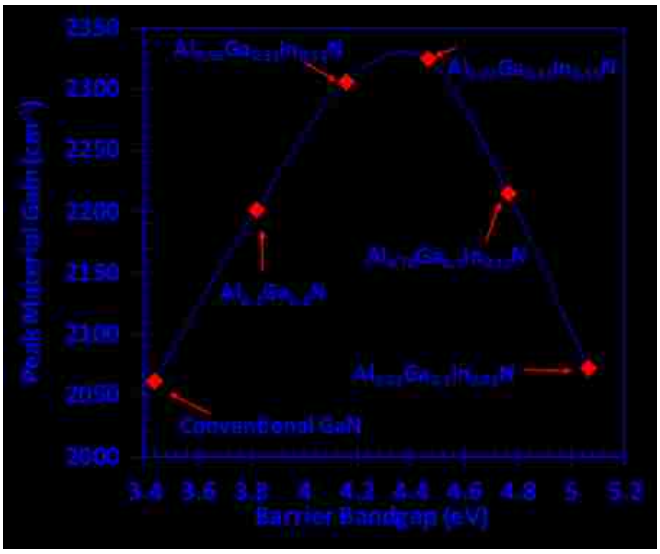

Figure 4-8: Peak material gain versus increasing barrier bandgap (eV) for 24-Å $In_{0.28}Ga_{0.72}N$-GaN QW (3.437eV), 24-Å $In_{0.28}Ga_{0.72}N$-$Al_{0.2}Ga_{0.8}N$ QW (3.822eV), 24-Å $In_{0.28}Ga_{0.72}N$-$Al_{0.56}Ga_{0.32}In_{0.12}N$ QW (4.156eV), 24-Å $In_{0.28}Ga_{0.72}N$-$Al_{0.72}Ga_{0.13}In_{0.15}N$ QW (4.465eV), 24-Å $In_{0.28}Ga_{0.72}N$-$Al_{0.78}Ga_{0.1}In_{0.12}N$ QW (4.765eV), and 24-Å $In_{0.28}Ga_{0.72}N$-$Al_{0.82}Ga_{0.1}In_{0.08}N$ QW (5.065eV). The carrier density is calculated at n=6× $10^{19} cm^{-3}$.

In Figure 4-8, we plot the peak value of material gain versus increasing barrier bandgap (eV) for 24-Å $In_{0.28}Ga_{0.72}N$-GaN QW (3.437eV), 24-Å $In_{0.28}Ga_{0.72}N$-$Al_{0.2}Ga_{0.8}N$ QW (3.822eV), 24-Å $In_{0.28}Ga_{0.72}N$-$Al_{0.56}Ga_{0.32}In_{0.12}N$ QW (4.156eV), 24-Å $In_{0.28}Ga_{0.72}N$-$Al_{0.72}Ga_{0.13}In_{0.15}N$ QW (4.465eV), 24-Å $In_{0.28}Ga_{0.72}N$-$Al_{0.78}Ga_{0.1}In_{0.12}N$ QW (4.765eV), and 24-Å $In_{0.28}Ga_{0.72}N$-$Al_{0.82}Ga_{0.1}In_{0.08}N$ QW (5.065eV). The carrier density is calculated at n=6× $10^{19} cm^{-3}$. The figure shows a parabolic shape for barrier bandgap from 3.43eV-5.06eV, which indicates that we can have an optimized

1-nm strain compensated barrier between the bandgap of 4.2eV and 4.4eV for the best gain properties.

4.3 Summary

In this chapter, we investigate the spontaneous emission characteristics and gain optical gain characteristics of the conventional and strain-compensated QWs. The spontaneous emission rate is much larger in low carrier density regime for strain-compensated QWs than the conventional QW. However, the enhancement factor of the spontaneous emission rate is smaller in the high carrier density regime than that in the low carrier density regime. The optical gain of the strain-compensated QWs is larger than that of the conventional QW. The increased electron and hole wave function overlap due to the better carrier confinement from the AlGaInN barriers results in an improvement of the spontaneous emission rate. The enhancement of spontaneous emission and gain properties can be utilized to achieve better optical properties for lasers and LEDs.

In this chapter, we also draw the conclusion that peak spontaneous emission rate and peak material gain follow a parabolic shape with an increasing AlGaInN barrier bandgap ranging from 3.43eV-5.06eV. An optimized 1-nm strain-compensated barrier for 24-Å $In_{0.28}Ga_{0.72}N$-AlGaInN QWs can be obtained between the bandgaps of 4.2 eV to 4.4 eV.

Chapter 5: Conclusion

In conclusion, this thesis presents a self-consistent simulation study on the spontaneous emission and optical gain properties of various strain-compensated InGaN–AlGaInN QWs as active regions for lasers and LEDs with indium content of 28%. In Chapter 1 we presented an introduction of InGaN-based semiconductors along with current technological challenges and the concept of strain-compensated quantum wells. We followed this by presenting the self-consistent 6-band ***k·p*** method in Chapter 2. The Chapter 3 focused on the band properties of conventional and various strain-compensated quantum well structures. Finally, in Chapter 4 we investigated the optical properties of the conventional and strain-compensated quantum wells.

From our analysis, both the spontaneous emission spectra and optical gain of strain-compensated InGaN–AlGaInN QWs reveal significant enhancement in comparison to those of conventional InGaN–GaN QWs. The strain-compensated InGaN-AlGaInN QWs exhibit 60%-180% enhancement of the spontaneous emission radiative recombination rate for carrier densities in the low carrier density regime (from $n = 1 \times 10^{18} cm^{-3}$ up to $n = 10 \times 10^{18} cm^{-3}$), which is serviceable for LED operation. At high carrier densities ($n = 2 \times 10^{19} cm^{-3}$ up to $n = 6 \times 10^{19} cm^{-3}$), the spontaneous emission radiative recombination rate of strain-compensated 24-Å $In_{0.28}Ga_{0.72}N$-$Al_{0.2}Ga_{0.8}N$ QW, 24-Å $In_{0.28}Ga_{0.72}N$-$Al_{0.56}Ga_{0.32}In_{0.12}N$ QW, and 24-Å $In_{0.28}Ga_{0.72}N$- $Al_{0.78}Ga_{0.1}In_{0.12}N$ QW are found to be enhanced 22%(12%), 35%(19%), and 32%(16%) at transparency and threshold conditions, respectively. The strain-compensated 24-Å $In_{0.28}Ga_{0.72}N$-$Al_{0.2}Ga_{0.8}N$ QW, 24-Å $In_{0.28}Ga_{0.72}N$-$Al_{0.56}Ga_{0.32}In_{0.12}N$ QW, and 24-Å $In_{0.28}Ga_{0.72}N$-$Al_{0.78}Ga_{0.1}In_{0.12}N$ QW also exhibit improvements of 12.2%, 16.6%, and 14.2%, respectively, for the

peak optical gain in comparison to that of conventional InGaN-GaN QW. This finding shows the potential of a reduction in the threshold carrier density for strain-compensated InGaN-AlGaInN QW active region. Our study shows a parabolic shape of peak spontaneous emission rate and peak material gain with increasing barrier bandgap ranges from 3.43eV-5.06eV. This indicates that one can achieve the best properties for this material system by fabricating an optimized 1-nm strain compensated barrier for 24-Å $In_{0.28}Ga_{0.72}N$-AlGaInN QWs between the bandgaps of 4.2eV and 4.4eV. This finding will provide a useful guidance for experimentalist to pursue the usage of InGaN-AlGaInN QW system as a possible active region for achieving improved spontaneous emission rate and optical gains for nitride-based photonics devices.

References

[1] J.I. Pankove, E.A. Miller, and J.E. Berkeyheiser, "GaN electroluminescent diodes," *RCA Rev*., vol. 32, pp. 383, Oct. 1971.

[2] H.M. Manasevit, "The use of metalorganics in the preparation of semiconductor materials: growth on insulating substrates," *J. of Crys*. *Gro.*, vol. 118, pp. 306-314, Apr. 1972**.**

[3] T. kawabata, T. Matsuda, and S.Koike, "GaN blue light emitting diodes prepared by metalorganic chemical vapor deposition," *J. of Appl. Phys.*, vol. 56, pp. 2367, May 1984.

[4] H. Amano, M. Kitoh, K. Hiramatsu, and I. Akasaki. *Inst Phys Conf Ser No 106*: Chapter 10.

[5] S. Nakamura*,* M. Senoh*, and* T. Mukai, "High-power InGaN/GaN double-heterostructure violet light emitting diodes", *Appl. Phys. Lett.*, vol. 62, pp. 2390, Feb. 1993.

[6] I. Akasaki, H. Amano, S. Sota, H. Sakai, T.Tanaka, and M. Koike, " Stimulated emission by current injection from an AlGaN/GaN/GaInN quantum well device", *Jpn. J. Appl. Phys.*, vol. 34, pp. 1517, Aug. 1995.

[7] "The Nobel Prize in Physics 2014". [Online]. Available: https://www.nobelprize.org/nobel_prizes/physics/laureates/2014/. [Accessed: 10-Dec-2017].

[8] H.P.Zhao, R.A. Arif, Y.Khoon Ee, and N.Tansu, "Self-consistent analysis of strain-compensated InGaN-AlGaN quantum wells for lasers and light-emitting diodes,"*IEEE*

J.Quantum Electron., vol.45, no.1, pp.66-78, Jan. 2009.

[9] N. Tansu, N. J. Kirsch, and L. J. Mawst, "Low-threshold-current-density 1300-nm dilute-nitride quantum well lasers," *Appl. Phys. Lett.*, vol. 81, pp. 2523–2525, Sep. 2002.

[10] N. Tansu, J. Y. Yeh, and L. J. Mawst, "Extremely low threshold-current-density InGaAs quantum well lasers with emission wavelength of 1215–1233 nm," *Appl. Phys. Lett.*, vol. 82, pp. 4038–4040, Jun. 2003.

[11] N. Tansu, J. Y. Yeh, and L. J. Mawst, "Physics and characteristics of 1200-nm InGaAs and 1300–1400 nm InGaAsN quantum-well lasers by metalorganic chemical vapor deposition," *IOP J. Physics: Condens. Matter Phys.*, vol. 16, pp. S3277–S3318, Aug. 2004.

[12] S. J. Chang, C. H. Kuo, Y. K. Su, L. W. Wu, J. K. Sheu, T. C. Wen, W. C. Lai, J. F. Chen, and J. M. Tsai, "400-nm InGaN-GaN and InGaN-AlGaN multiquantum well light-emitting diodes," *IEEE J. Sel. Topics Quantum Electron.*, vol. 8, no. 4, pp. 744–748, Aug. 2002.

[13] N. Tansu, J. Y. Yeh, and L. J. Mawst, "Experimental evidence of carrier leakage in InGaAsN quantum well lasers," *Appl. Phys. Lett.*, vol. 83, pp. 2112–2114, Sep. 2003.

[14] N. Tansu and L. J. Mawst, "Current injection efficiency of 1300-nm InGaAsN quantum-well lasers," *J. Appl. Phys.*, vol. 97, pp. 2523–2525, Mar. 2005.

[15] T. Fukunaga, M. Wada, and T. Hayakawa, "Reliable operation of strain-compensated 1.06 m InGaAs/InGaAsP/GaAs single quantum well lasers," *Appl. Phys. Lett.*, vol. 69, pp. 248–250, Jul. 1996.

[16] S. L. Chuang and C. S. Chang, "$\boldsymbol{k \cdot p}$ method for strained wurtzite semiconductors," *Phys.*

Rev. B., vol. 54, pp. 2491–2504, Jul. 1996

[17] S. L. Chuang, “Optical gain of strained wurtzite GaN quantum-well lasers,” *IEEE J. Quantum Electron.*, vol. 32, no. 10, pp. 1791–1800, Oct. 1996.

[18] C. Kittel, "*Quantum Theory of Solids* (Second Revised Printing ed.)", New York: Wiley. pp. 186–190. ISBN 0-471-62412-8

[19] F. Bernardini and V. Fiorentini, “Spontaneous versus piezoelectric polarization in III–V Nitrides: Conceptual aspects and practical consequences,” *Phys. Stat. Sol. (b)*, vol. 216, pp. 391–398, Nov. 1999.

[20] O. Ambacher, J. Majewski, C. Miskys, A. Link, M. Hermann, M. Eick-hoff, M. Stutzmann, F. Bernardini, V. Fiorentini, V. Tilak, W. J. Schaff, and L. F. Eastman, “Pyroelectric properties of Al(In)GaN/GaN hetero and quantum well structures,” *J. Phys.: Condens. Matter*, vol. 14, pp. 3399–3434, Mar. 2002.

[21] I. Vurgaftman and J. R. Meyer, “Band parameters for nitrogen-containing semiconductors,” *J. Appl. Phys.*, vol. 94, pp. 3675–3696, Sep. 2003.

[22] S. L. Chuang, Physics of Optoelectronics Devices. New York: Wiley, 1995, ch. 4 and 9

[23] S. L. Chuang and C. S. Chang, “A band-structure model of strained quantum-well wurtzite semiconductors,” *Semicond. Sci. Technol.*, vol. 12, pp. 252–263, 1997

[24] M.Rowe, P.Michler, J.Gutowski, V. Kummler, A.Lell, and V.Harle, "Influence of the carrier density on the optical gain and refractive index change in InGaN laser strucuture," *Phys.Stat.Solid(A)*, vol.200, pp. 135-138, Sep.2003

Vita

Hanlin Fu was born on February 3, 1993, in Dalian, China to Shouchen Fu and Yuehua Pei. He entered the University of Science and Technology of China in 2011 and graduated with a Bachelor's of Science in Atomic and Molecular Physics. He did research projects in Chinese Academy of Science as a research assistant from September 2015 to June 2016. He started his graduate studies in Electrical Engineering at Lehigh University under his adviser Professor Nelson Tansu in 2016. With this thesis, he will graduate with a Master's of Science in Electrical Engineering in December 2017.